# Planar Chiral Copper(I) Complexes Realize Efficient Circularly Polarized Electroluminescence

Ao Ying [a], Lisi Zhan [a], Yao Tan [a], Xiaosong Cao [b], Chuluo Yang [b] and Shaolong Gong [a] *

a)      A. Ying, L. Zhan, Y. Tan, Prof. Dr. S. Gong
Department of Chemistry, Hubei Key Lab on Organic and Polymeric Optoelectronic Materials, Wuhan University
Wuhan 430072, China
E-mail: slgong@whu.edu.cn
b)      Dr. X. Cao, Prof. Dr. C. Yang
Shenzhen Key Laboratory of Polymer Science and Technology, College of Materials Science and Engineering, Shenzhen University,
Shenzhen 518060, China

## Abstract

Chiral organometallic emitters hold great promise in potential and practical applications of circularly polarized organic light-emitting diodes (CP-OLEDs). However, developing luminescent earth-abundant organometallic complexes concurrently exhibiting circularly polarized luminescence (CPL) and high quantum efficiency remain a formidable challenge. In this study, we introduced a typical planar chiral skeleton of a [2.2]paracyclophane moiety into earth-abundant copper(I) complexes with the goals of realizing efficient CPL and thermally activated delayed fluorescence (TADF) simultaneously. Two pairs of proof-of-the-concept copper(I) enantiomers, $R_P/S_P$-MAC*-Cu-CzP and $R_P/S_P$-MAC*-Cu-CNCzP, were developed using planar chiral [2.2]paracyclophane-based donor ligands in a carbene-metal-amide (CMA) motif. Both panels of enantiomers not only exhibited significant mirror-image CPL signals but also displayed distinct TADF nature with fast reverse intersystem crossing rates of up to $10^8$ s$^{-1}$. The resultant OLEDs based on the MAC*-Cu-CzP enantiomers manifested efficient circularly polarized electroluminescence with excellent external

quantum efficiencies of 13.2% with ultraslow efficiency roll-off (7.7% at 10000 nits). This work not only demonstrates one of the best performance for CP-OLEDs based on earth-abundant organometallic complexes but also represents the first example of CP-OLEDs from CMA complexes to our knowledge.

**Introduction**

Recently chiral molecules exhibiting circularly polarized luminescence (CPL) have drawn paramount attentions due to their potential applications in 3D displays, optical sensors, and information storage.[1-4] Particularly, circularly polarized electroluminescence (CPEL) from circularly polarized organic light-emitting diodes (CP-OLEDs) have emerged out as a promising candidate for new-generation displays and lighting. The chiral emitters applied in CP-OLEDs can be roughly divided into three types: chiral polymers, chiral organic small molecules, and chiral organometallic complexes. Among them, chiral luminescent organometallic complexes that are usually constructed based on transition metals are more promising candidates for high-efficiency CP-OLEDs because of their superior merits of achieving high electroluminescence dissymmetry factor ($g_{EL}$) values and harnessing triplet excitons simultaneously.[5-8] For instance, Yang et al. developed efficient chiral iridium(III) complexes and their CP-OLEDs achieved satisfactory $g_{EL}$ of close to $10^{-2}$ and outstanding external quantum efficiency (EQE) of up to 30.6% (**Figure 1**).[9] Zheng and co-workers developed a pair of chiral platinum(II) complexes and the respect CP-OLEDs exhibited high $g_{EL}$ values of up to $5.1\times10^{-3}$ along with outstanding EQE of up

to 18.8%.[10] CPEL properties of europium(III) complexes were firstly studied by Bari et al. These europium(III) complexes exhibited sharp EL spectra with a maximum $g_{EL}$ value of up to 0.79, but delivered very poor device performance with a maximum EQE of 0.0042%.[11] Albeit the above impressive advances, the high cost and low earth abundance of precious and rare-earth metals limited their practical applications in CP-OLEDs. In this context, luminescent chiral organometallic complexes from earth-abundant metals are regarded as the more promising CPL-active emitters for CP-OLEDs. Despite the broad interest in the use of luminescent earth-abundant organometallic complexes in photocatalysis,[12,13] bioimaging,[14] and cluster luminescence,[15,16] their CPL and CPEL properties are rarely investigated. Up to now, only a few CPL-active zinc(II) and copper(I) complexes have been reported. Tang et al. firstly studied the CPEL properties of chiral salen-zinc(II) complexes with $g_{EL}$ of up to 0.044 (**Figure 1**), yet their device performance was unsatisfactory (the current efficiency of 0.18 cd A$^{-1}$).[17] In 2019, Ung et al. reported CPL-active copper(I) complexes with a photoluminescence dissymmetry factor ($g_{PL}$) of 0.0011, but they did not fabricate CP-OLEDs.[18] Very recently, Steffen et al. reported CP-OLEDs based on Cu(I) complexes to exhibit intense CPEL, yet the device performance was not reported.[19] Therefore, the search for new classes of efficient chiral earth-abundant metal complexes is of vital importance for high-performance and cost-effective CP-OLEDs.

Recently luminescent Cu(I) complexes based on a two-coordinate carbene-metal-amide (CMA) motif have been rapidly developed as the new-generation emitters for

high-performance and cost-effective OLEDs.[20-30] Thanks to the formation of excited states with large ligand-to-ligand charge-transfer (LLCT) character and small metal feature as well as the linear geometry and coplanar conformation,[31] most Cu(I)-CMA complexes show high quantum efficiencies, distinct thermally activated delayed fluorescence (TADF) nature, and high radiative rate constants ($k_r \sim 10^6\,\text{s}^{-1}$). To date, the reported Cu(I)-CMA-based OLEDs have achieved over 20% EQEs with small efficiency roll-offs.[26-30] Albeit the promising progress, the CPL-active Cu(I)-CMA complexes are rarely reported. Very recently we reported the first example of CPL-active Cu(I)-CMA complexes by using chiral carbene ligands in the CMA motif.[32] Despite the realization of distinct CPL in aggregation state, the reported chiral Cu(I)-CMA complexes exhibited undetectable or weak CPL signals in solution and film state. To the best of our knowledge, the CPEL properties of Cu(I)-CMA complexes are virtually unknown.

The [2.2]paracyclophane is a typical planar chiral moiety in asymmetric catalysis and chiral materials.[33] The previous studies also reveal that the [2.2]paracyclophane unit is an excellent fragment in design of CPL-active molecules.[34-36] In this study, we developed two planar chiral Cu(I) complexes, **MAC\*-Cu-CzP** and **MAC\*-Cu-CNCzP**, using [2.2]paracyclophane-based carbazole derivatives, $1^9$H-1(1,4)-carbazola-4(1,4)-benzenacyclohexaphane (CzP) and $1^9$H-1(1,4)-carbazola-4(1,4)-benzenacyclohexaphane-16-carbonitrile (CNCzP), as donor ligands with planar chirality in the CMA motif (**Figure 2A**). The [2.2]paracyclophane moiety not only serves as the chiral unit but also leads to a slightly bent geometry and a twisted

conformation stemming from the large steric hindrance between the carbene and amide ligands. The resultant Cu(I) complexes exhibited small $\Delta E_{ST}$ values and ultrafast reverse intersystem crossing (RISC) rates of up to $10^8$ s$^{-1}$ in diluted solutions. Thanks to the efficient chirality transfer from the planar chiral donor to the CMA Cu(I) complexes, $\textbf{\textit{R}}_{\textbf{\textit{p}}}$/$\textbf{\textit{S}}_{\textbf{\textit{p}}}$-$\textbf{MAC}^{\textbf{*}}$-$\textbf{Cu-CzP}$ showed obvious CPL signals with g$_{PL}$ values in the $10^{-4}$ order. On the basis of the CPL properties, we fabricated the first example of CP-OLEDs based on CMA complexes by using $\textbf{\textit{R}}_{\textbf{\textit{p}}}$/$\textbf{\textit{S}}_{\textbf{\textit{p}}}$-$\textbf{MAC}^{\textbf{*}}$-$\textbf{Cu-CzP}$ as emitters. The respect devices exhibited distinct CPEL signals with g$_{EL}$ values of +4.5 ×10$^{-4}$ and −5.9 ×10$^{-4}$, respectively. More importantly, the optimal devices based on $\textbf{MAC}^{\textbf{*}}$-$\textbf{Cu-CzP}$ exhibited a maximum EQE of 13.2% and delivered an extremely small efficiency roll-off of 7.7% at 10000 nits, among the highest performance for CP-OLEDs based on earth-abundant organometallic complexes.
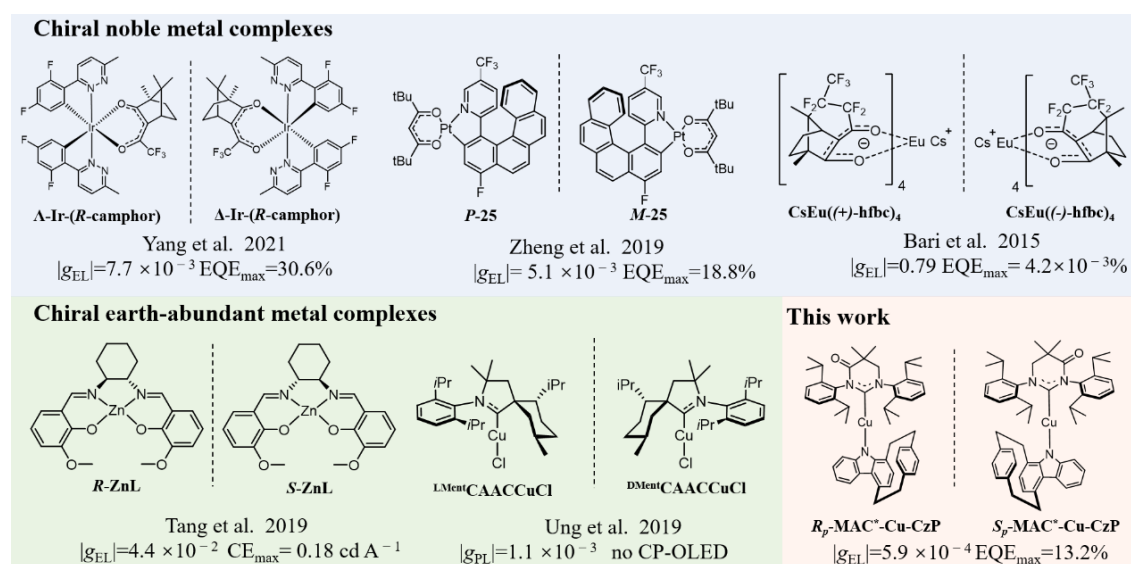


**Figure 1.** Selected examples of chiral organometallic emitters in the literature and chiral Cu(I) complexes in this work.
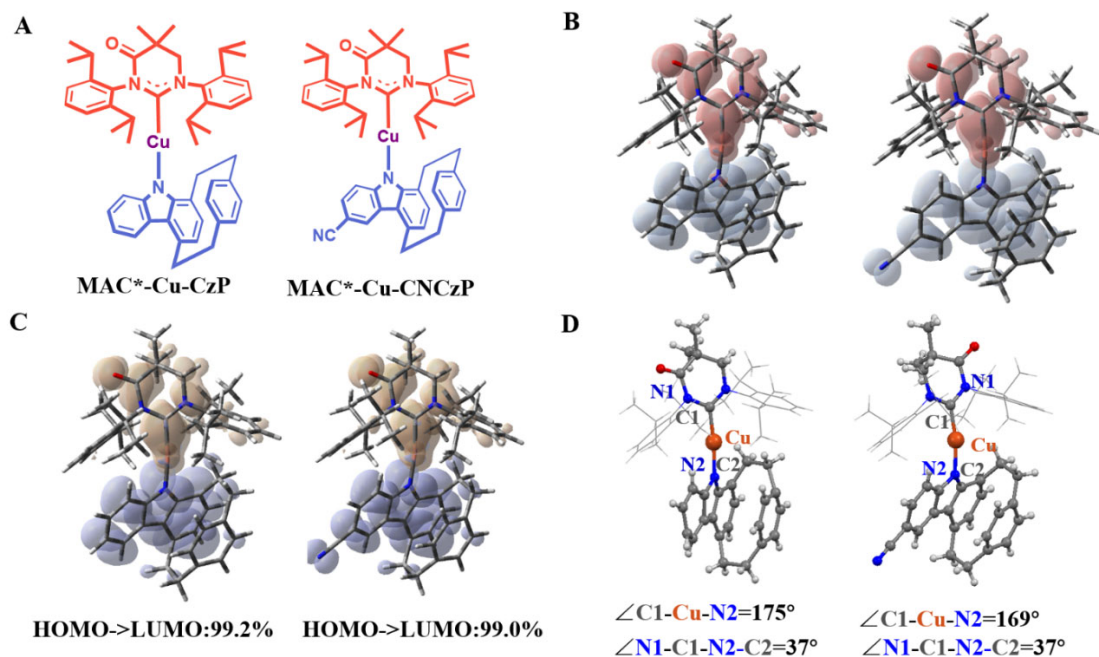
**Figure 2.** (A) Chemical structures. (B) HOMO/LUMO distributions (HOMO is shown in blue and LUMO is shown in red). (C) Calculated natural transition orbitals (NTO) distributions and relevant orbital components with the optimized structures of $S_1$ states of **MAC*-Cu-CzP** and **MAC*-Cu-CNCzP** (hole is shown in purple and particle is shown in yellow). The theoretical calculations shown here were all based on the $R_p$ conformations for Cu(I) complexes. (D) Single-crystal structures of $R_p$-**MAC*-Cu-CzP** and $R_p$-**MAC*-Cu-CNCzP**.

## Results and Discussion

## Molecular Design and Characterization

Density functional theory (DFT) and time-dependent DFT (TD-DFT) calculations were conducted on **MAC*-Cu-CzP** and **MAC*-Cu-CNCzP** to study their FMO distributions and electronic structures. As depicted in **Figure 2B**, the HOMOs and LUMOs of both complexes were principally located on the amide (CzP/CNCzP) and carbene ligands, respectively. Only a small FMO overlap was observed on the Cu(I) center and the N atom of the amide ligand. The complete separation of the FMOs resulted in small $\Delta E_{ST}$ values (~0.10 eV), implied the potential TADF properties of these complexes. Intriguingly, both complexes took twisted ground-state geometries

with a certain extent of torsion between the carbene and amide ligands (the twist angles of 34° for **MAC*-Cu-CzP** and 37° for **MAC*-Cu-CNCzP**). Such twisted conformation stemmed from significantly enhanced steric hindrance between the [2.2]paracyclophane-based amide ligand and the diisopropyl phenyl (Dipp) moiety of the carbene ligand. Moreover, the introduction of the [2.2]paracyclophane unit slightly lifted donor strength of the amide ligands. The calculated HOMO energy levels of CzP ($-5.51$ eV) and CNCzP ($-5.93$ eV) lies 0.18 and 0.27 eV shallower than that of carbazole ($-5.69$ eV) and 3-cyanocarbazole ($-6.20$ eV), respectively (**Figure S1**). According to natural transition orbital (NTO) analysis (**Figure 2C**), the $S_1$ excited states of both complexes were dominated by ligand-ligand charge transfer (LLCT) together with >99% HOMO-LUMO contributions. It is noteworthy that the hole of $S_1$ states distributed to the methylene and phenyl of the [2.2]paracyclophane unit, indicating the promising chirality transfer from the [2.2]paracyclophane-based donor to the CMA system. On the other hand, the introduction of the [2.2]paracyclophane unit slightly decreased the CT-featured $S_1$ energy levels of **MAC*-Cu-CzP** (2.02 eV, 614 nm) and **MAC*-Cu-CNCzP** (2.35 eV, 528 nm) compared with that of their carbazole-based counterparts (MAC*)Cu(Cz) (2.19 eV, 566 nm) and (MAC*)Cu(CNCz) (2.47 eV, 502 nm), respectively (**Figure S1**).[23]

The [2.2]paracyclophane-based donor ligands CzP and CNCzP were synthesized from 1,4(1,4)-dibenzenacyclohexaphan-1-amine via a two-step route including Pd-catalyzed C-N coupling and Pd-catalyzed intramolecular cyclization reactions (**Scheme S1).** Both Cu(I) complexes were prepared by a simple and catalyst-free nucleophilic reaction

between the key intermediate of MAC*CuCl and corresponding donor ligands with NaH as the base (**Scheme S2**). The chemical structures of the Cu(I) complexes were characterized by $^1$H/$^{13}$C nuclear magnetic resonance spectroscopy and high resolution mass spectrometry. Enantiomeric complexes were obtained in the same methods but using enantiomeric pure CzP/CNCzP ligands conducted by chiral high performance liquid chromatography (**Scheme S3**, **Figures S2** and **S3**). X-ray crystallographic analysis were further performed to confirm the molecular structures of these complexes (**Figure 2D** and **Table S1**).[37] ***R*$_p$-MAC\*-Cu-CzP** and ***R*$_p$-MAC\*-Cu-CNCzP** delivered C-Cu and Cu-N bond lengths of 1.90 and 1.89 Å, respectively, slightly longer than those of most previously reported Cu(I)-CMA complexes (C-Cu: 1.87 Å; Cu-N: 1.86 Å). Meanwhile, both complexes preferred twisted conformations along with ligand-ligand dihedral angles of 37° (**Figure 2D**). Furthermore, the conformations of ***R*$_p$-MAC\*-Cu-CzP** and ***R*$_p$-MAC\*-Cu-CNCzP** were not absolutely linear, but possessing bent angles of 5° and 11°, respectively. In comparison with typical CMA complexes having linear and coplanar conformation, such structural uniqueness pinpointed that the $N_{Cz}$ of both complexes deviated from the typical sp$^2$-hybridized coordination.[38] This was further supported by the sum of bonding angles around the $N_{Cz}$ of ***R*$_p$-MAC\*-Cu-CzP** (358.1°) and ***R*$_p$-MAC\*-Cu-CNCzP** (354.2°).

**MAC\*-Cu-CzP** and **MAC\*-Cu-CNCzP** were thermally stable with relatively high decomposition temperatures of 314 °C and 334 °C, respectively (**Figure S4**), making them feasible to a high-vacuum sublimation. The cyclic voltammetry study revealed that both **MAC\*-Cu-CzP** and **MAC\*-Cu-CNCzP** undergone donor-attributed

irreversible oxidation processes (**Figure S5**) along with the half-wave potentials of +0.68 V and +0.77 V (calibrated versus ferrocenium/ferrocene), respectively. In combination with optical band gaps, the HOMO/LUMO levels of **MAC\*-Cu-CzP** and **MAC\*-Cu-CNCzP** were determined to be −5.47/−2.86 eV and −5.54/−2.64 eV, respectively.
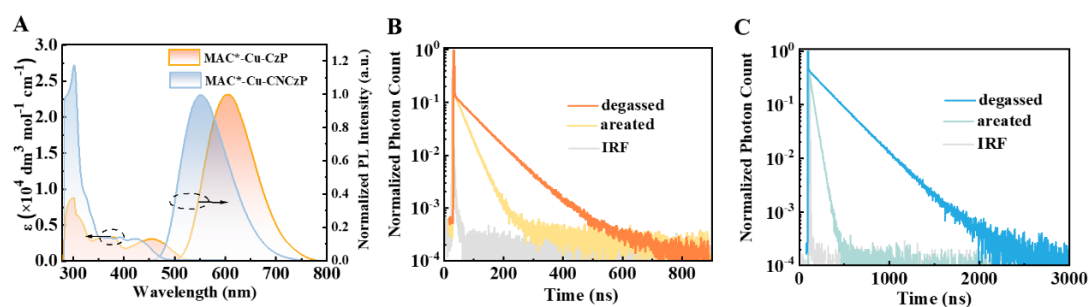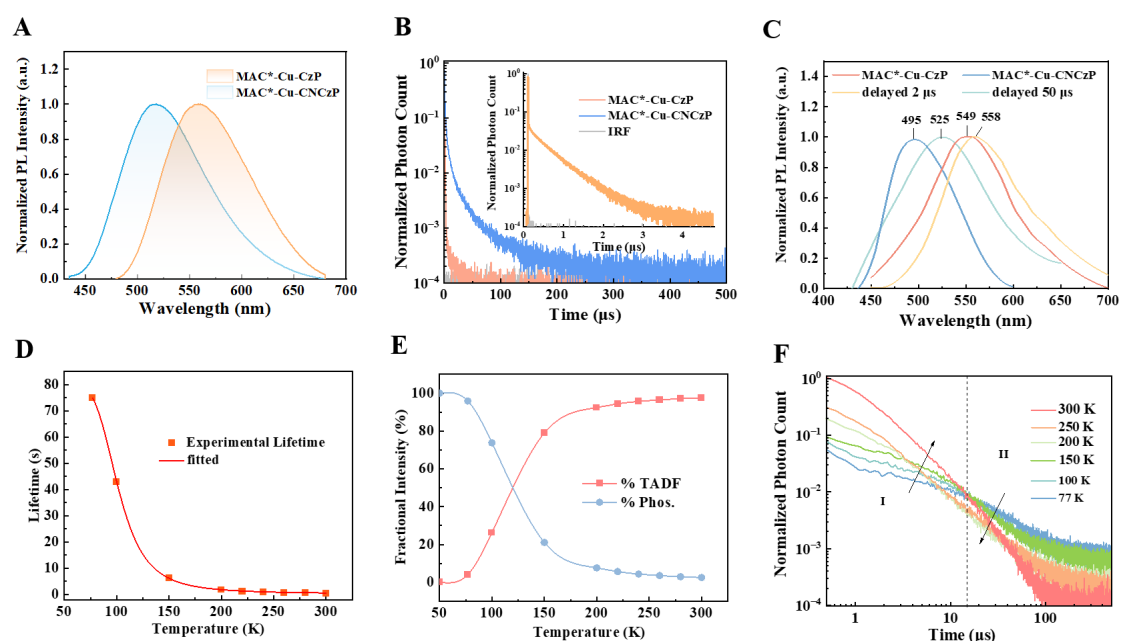


**Figure 3.** (A) UV-vis absorption and normalized fluorescence spectra of **MAC\*-Cu-CzP** and **MAC\*-Cu-CNCzP** in toluene ($1 \times 10^{-4}$ M, 300 K). Transient PL decay curves of (B) **MAC\*-Cu-CzP** and (C) **MAC\*-Cu-CNCzP** in toluene ($1 \times 10^{-4}$ M, 300 K).

**Photophysical Properties**

As illustrated in **Figure 3A**, besides strong ligand-attributed absorption bands with the edge around 400 nm, weak absorption bands at 400-600 nm ($\varepsilon = 1.2 \times 10^3$ dm$^3$ mol$^{-1}$ cm$^{-1}$) of these complexes belonged to LLCT transition from the CzP/CNCzP donor to the MAC$^*$ acceptor. Both **MAC$^*$-Cu-CzP** and **MAC$^*$-Cu-CNCzP** exhibited broad and structureless emissions peaking at 607 and 551 nm, respectively. Both complexes in degassed toluene exhibited a double exponential decay profile composed of ps-scale ISC-dominant component (shown in **Figure S6**) and sub-μs-scale radiation (**Figure 3B**, **3C** and **Table S2**). Impressively, **MAC$^*$-Cu-CzP** exhibited an ultrashort decay lifetime ($\tau_d$) of 88 ns compared with that of **MAC$^*$-Cu-CNCzP** (254 ns). According to the

Strickler-Berg analysis (**eq. S7** and **Table 1**), **MAC*-Cu-CzP** and **MAC*-Cu-CNCzP** had almost the same singlet radiative rate constants ($k_{r,s}$) of $1.46 \times 10^7$ s$^{-1}$ (68 ns) and $1.47 \times 10^7$ s$^{-1}$ (69 ns), respectively. Such constant was close to the detected emissive lifetime of **MAC*-Cu-CzP** (88 ns), implying its ultrafast spin-flip ($k_{RISC} = 1.46 \times 10^8$ s$^{-1}$) from T$_1$ to S$_1$. Comparatively, **MAC*-Cu-CNCzP** undergone a slow RISC process ($k_{RISC} = 8.7 \times 10^6$ s$^{-1}$), making it the rate-determined step.



**Figure 4.** (A) Normalized fluorescence spectra of 3.0 wt% **MAC*-Cu-CzP** and **MAC*-Cu-CNCzP** doped into the mCBP host at 300 K. Transient PL decay curves of (B) **MAC*-Cu-CzP** and **MAC*-Cu-CNCzP** in 3.0 wt% mCBP-doped film at 300 K. Inset: transient PL decay curve of **MAC*-Cu-CzP** in a 5 μs time range. (C) Time-resolved emission spectra of **MAC*-Cu-CzP** and **MAC*-Cu-CNCzP** in 3.0 wt% mCBP-doped film at 300 K. (D) Temperature-dependent lifetimes of **MAC*-Cu-CzP**, the detected lifetimes were fitted to **eq. S4**. (E) Temperature-dependent TADF and phosphorescence fractional intensities of **MAC*-Cu-CzP**. (F) Temperature-dependent transient PL decay curves of **MAC*-Cu-CNCzP**.

**Table 1.** Photophysical properties of **MAC*-Cu-CzP** and **MAC*-Cu-CNCzP** in the mCBP-doped films and toluene.

| compound | $\lambda_{PL}$ [nm] [a] | $\tau_d$ [μs] [a] | $\Phi_{PL}$ [%][a] | $\Delta E_{ST}$[b] [eV] | $k_{r,s}$[c] [$10^7$ s$^{-1}$] | $k_r$[d]/ $k_{nr}$[e] [$10^5$ s$^{-1}$] | $k_{ISC}$[f]/$k_{RISC}$[g] [$10^7$ s$^{-1}$] |
|---|---|---|---|---|---|---|---|
| MAC*-Cu-CzP | 559 | 0.4 | 40 | 0.06 | 1.46 | 11.7/17.5 | 340/14.6 |
| MAC*-Cu-CNCzP | 518 | 2.58 (77%) 34.1 (23%) | 48 | 0.11 | 1.47 | 0.5/1.1 | 610/0.87 |

[a] Obtained in mCBP-doped films with 3 wt.% doping concentration. [b] Obtained from the fit to the two-level Boltzmann model (**eq. S4**) in the mCBP-doped films. [c] Estimated from the Strickler-Berg analysis based on the absorption and emission spectra in toluene. [d] $k_r = \Phi_{PL}/\tau_d$. [e] $k_{nr} = k_r/\Phi_{PL} - k_r$. [f] Measured in toluene. [g] Calculated based on the equilibrium constant (**eq. S3**) in toluene.

To evaluate conditions relevant to OLED device, we studied the emissive characteristics of **MAC*-Cu-CzP** and **MAC*-Cu-CNCzP** in the mCBP (1,3-di(9H-carbazol-9-yl)benzene) host. **MAC*-Cu-CzP** and **MAC*-Cu-CNCzP** exhibited CT-featured emission profiles peaking at 559 and 518 nm, together with moderate photoluminescence quantum yields of 40% and 48% in the doped films (**Figure 4A** and **Table 1**), respectively. Comparing with the photophysical behaviors in toluene, **MAC*-Cu-CzP** exhibited similar transient PL curves in the mCBP-doped film, along with a longer decay lifetime ($\tau_d$) of 0.4 μs (**Figure 4B** and **Table 1**). Differently, **MAC*-Cu-CNCzP** in the doped film displayed an exceptionally long decay radiation including two decay components ($\tau_1 = 2.58$ μs, 77%; $\tau_2 = 34.1$ μs, 23%) in a 500 μs time range (**Figure 4B** and **Table 1**). To clarify the origin of such a difference, we recorded the time-resolved emission spectra of both complexes in the mCBP host (**Figure 4C**). After a 2 μs delay, **MAC*-Cu-CzP** exhibited a slightly bathochromic from 549 (2.26 eV) to 558 nm (2.22 eV), which could be attributed to the energy relaxation to a quasi-equilibrium state.[38] Whereas, **MAC*-Cu-CNCzP** displayed a significant emission red-shift from 495 (2.51 eV) to 525 nm (2.36 eV) after a 50 μs delay. The 0.15 eV red-shift is much larger than normal energetic relaxation ($< 0.1$ eV) for CMA systems.[39,40]

Therefore, we envision that the direct phosphorescence could contribute to the emission of **MAC\*-Cu-CNCzP**. Subsequently, we performed temperature-dependent lifetimes for these complexes in the mCBP host (**Figures S7-S9** and **Table S3-S4**). As shown in **Figure 4D**, when cooling down to 77 K, **MAC\*-Cu-CzP** exhibited two orders of magnitude longer average decay lifetime (75.0 μs) than that at 300 K (0.4 μs). Combining with the estimated large radiative rate constant ($k_r = 1.17×10^6\,s^{-1}$), **MAC\*-Cu-CzP** had distinct TADF nature. In this sense, the phosphorescence channel of **MAC\*-Cu-CzP** was significantly suppressed at 300 K, along with a tiny fractional intensity of below 3% (**Figure 4E**). Comparatively, the decay curves of **MAC\*-Cu-CNCzP** at different temperatures exhibited clearly two distinct regions: the decay below 20 μs (region I) and the decay between 20 and 500 μs (region II). In region I, the emission intensities increased with the increasing temperature, establishing the TADF nature in this region; whereas region II had an inverse temperature dependence: the emission intensities decreased along with the rise of temperature, indicating the phosphorescence-dominated mechanism (**Figure 4E**). To unravel the origin of different photophysical behaviors of the complexes, we extracted some key parameters of exciton dynamics. As illustrated in **Figure S10**, **MAC\*-Cu-CNCzP** had larger spin-orbital coupling (SOC) constant between $T_1$ and $S_0$ (17.0 cm$^{-1}$) compared with **MAC\*-Cu-CzP** (14.1 cm$^{-1}$). Meanwhile, **MAC\*-Cu-CNCzP** exhibited shorter decay lifetime at 77 K (40.1 μs) than that of **MAC\*-Cu-CzP** (75.0 μs), suggesting the faster triplet radiative rate of **MAC\*-Cu-CNCzP**. In this context, the phosphorescent channel partially contributed to the emission of **MAC\*-Cu-CNCzP** in film state at 300 K due

to its stronger SOC between $T_1$ and $S_0$ and faster triplet radiative rate. Additionally, the larger $\Delta E_{ST}$ and faster intersystem crossing (ISC) rate of **MAC*-Cu-CNCzP (Table 1)** also facilitated the triplet accumulation and thus assisted phosphorescence radiation. The estimated lower $k_r$ ($5 \times 10^5$ s$^{-1}$) of **MAC*-Cu-CNCzP** was also consistent with the above results.
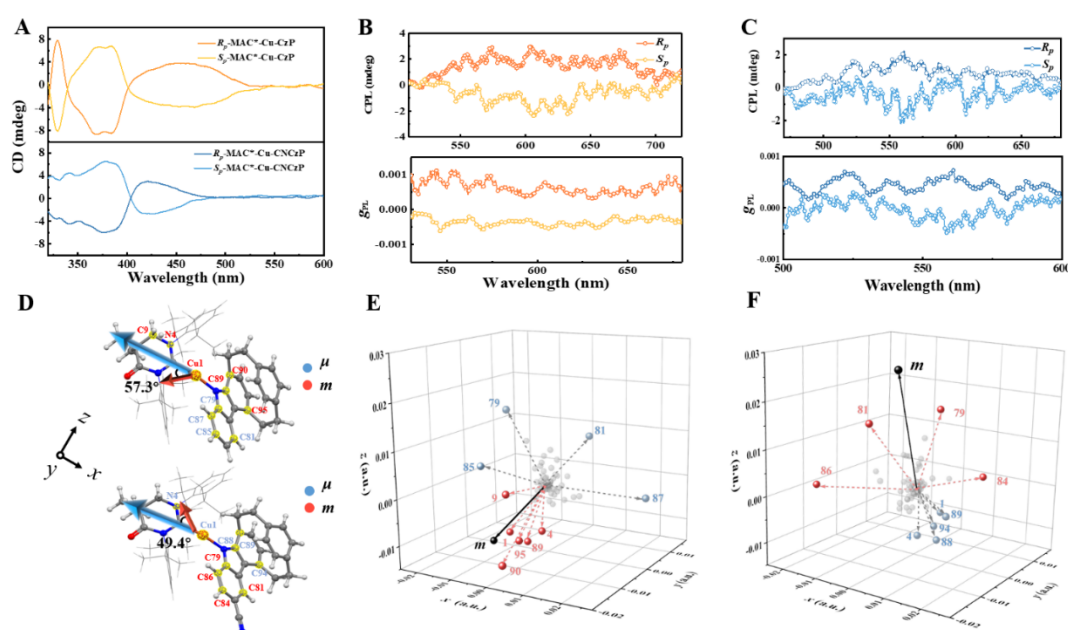


**Figure 5.** (A) Circular dichroism spectra of $R_p/S_p$-**MAC*-Cu-CzP** and $R_p/S_p$-**MAC*-Cu-CNCzP** in toluene ($10^{-3}$ M, 300 K). Circularly polarized luminescence spectra and photoluminescence dissymmetry factors of (B) $R_p/S_p$-**MAC*-Cu-CzP** and (C) $R_p/S_p$-**MAC*-Cu-CNCzP** in $10^{-4}$ M toluene. (D) Transition dipole moments and atom coordinates of $R_p$-**MAC*-Cu-CzP** and $R_p$-**MAC*-Cu-CNCzP**. Atomic contribution to the magnetic transition dipole moments of (E) $R_p$-**MAC*-Cu-CzP** and (F) $R_p$-**MAC*-Cu-CNCzP**.

**Table 2.** Parameters of simulated electric ($|\boldsymbol{\mu}|$) and magnetic ($|\boldsymbol{m}|$) transition dipole moments for $R_p/S_p$-**MAC*-Cu-CzP** and $R_p/S_p$-**MAC*-Cu-CNCzP**.

| emitter | $\|\boldsymbol{\mu}\|$ [× 10$^{-18}$ esu cm] | $\|\boldsymbol{m}\|$ [× 10$^{-22}$ erg G$^{-1}$] | $R$ [× 10$^{-40}$ erg esu cm G$^{-1}$] | $\theta_{\mu,m}$ [deg] | $\|\boldsymbol{m}\|\cos\theta_{\mu,m}/$ $\|\boldsymbol{\mu}\|$ [10$^{-4}$] | $g_{cal}$ [10$^{-4}$] | $g_{PL}$[a] [10$^{-4}$] |
|---|---|---|---|---|---|---|---|
| $R_p$-MAC*-Cu-CzP | 2.22 | 5.38 | +6.45 | 57.3 | +1.77 | +7.08 | +6.2 |
| $S_p$-MAC*-Cu-CzP | 2.22 | 5.38 | −6.45 | 122.7 | −1.77 | −7.08 | −5.5 |
| $R_p$-MAC*-Cu-CNCzP | 2.38 | 4.14 | +6.41 | 49.4 | +1.13 | +4.52 | +3.4 |
| $S_p$-MAC*-Cu-CNCzP | 2.38 | 4.14 | −6.41 | 130.6 | −1.13 | −4.52 | −3.0 |

**Chiroptical Properties**

Considering potential chirality transfer from the planar chiral donor to the Cu(I) complexes, we studied chiroptical properties of $R_p$/$S_p$-**MAC***-**Cu-CzP** and $R_p$/$S_p$-**MAC***-**Cu-CNCzP** at the ground and excited states by circular dichroism (CD) and CPL spectra, respectively. $R_p$/$S_p$-**MAC***-**Cu-CzP** and $R_p$/$S_p$-**MAC***-**Cu-CNCzP** displayed clear mirror-image CD spectra in toluene (**Figure 5A**). The CD absorption below 350 nm belonged to the π-π* transition and typical absorption of the chiral donor ligands (**Figure S11**). Based on the simulated electronic CD spectra (**Figure S12**) and NTO analysis (**Figure S13**), the strong absorption bands at 370-400 nm could be ascribed to the absorption of higher-lying locally excited (LE) states hybridizing with metal-to-ligand charge transfer (MLCT). Such characteristic absorption implied the planar chirality of the amide ligand can be transferred through the Cu(I) center. The clearly monosignate Cotton effects were observed in the LLCT region for these complexes (400-550 nm for $R_p$/$S_p$-**MAC***-**Cu-CzP** and 405-480 nm for $R_p$/$S_p$-**MAC***-**Cu-CNCzP**), further confirming the efficient chirality transfer from the chiral CzP/CNCzP donor to the CMA motif at the ground state. The absorption dissymmetry factors ($g_{abs}$) of $R_p$/$S_p$-**MAC***-**Cu-CzP** and $R_p$/$S_p$-**MAC***-**Cu-CNCzP** at maximum peaks were calculated to be $+7.2 \times 10^{-4}$/$-7.5 \times 10^{-4}$ and $+6.3 \times 10^{-4}$/$-6.1 \times 10^{-4}$, respectively. Notably, $R_p$/$S_p$-**MAC***-**Cu-CzP** exhibited obvious mirror-symmetric CPL profiles both in toluene and the doped films (**Figures 5B** and **S14**), together with similar $g_{PL}$ values of $+6.2 \times 10^{-4}$/$-5.5 \times 10^{-4}$ in toluene and $+4.7 \times 10^{-4}$/$-3.8 \times 10^{-4}$ in doped films, respectively. This clearly establishes the chirality of the S$_1$ excited state of $R_p$/$S_p$-

**MAC\*-Cu-CzP**. Comparatively, $R_p$/$S_p$-**MAC\*-Cu-CNCzP** manifested weaker mirror-image CPL signals with inferior $g_{PL}$ values of $+3.4\times10^{-4}$/$-3.0\times10^{-4}$ in toluene (**Figure 5C**) and displayed undetectable CPL signal in the doped films.

To understand the chiroptical difference of these emitters, we conducted theoretical estimation on the electric (**$\mu$**) and magnetic (**$m$**) transition dipole moments. Theoretically, the calculated dissymmetry factor (**$g$**) could be estimated by the simplified equation below if $|\mu| \gg |m|$:

$$g = \frac{4|m|\cos\theta_{\mu,m}}{|\mu|}$$

In this sense, an ideal chiral emitter should possess large $|m|$ and $|\cos\theta_{\mu,m}|$ as well as small $|\mu|$ simultaneously to maximize $g$ value.[41] In our case, $R_p$/$S_p$-**MAC\*-Cu-CzP** and $R_p$/$S_p$-**MAC\*-Cu-CNCzP** had similar $|\mu|$ values of $2.22\times10^{-18}$ and $2.38\times10^{-18}$ esu cm, respectively. Meanwhile, a reasonable orientation was obtained for $R_p$/$S_p$-**MAC\*-Cu-CzP** and $R_p$/$S_p$-**MAC\*-Cu-CNCzP**, accompanied with similar vector angles $\theta_{\mu,m}$ of 57.3°/122.7° and 49.4°/130.6° (**Figure 5D**), respectively. Similar to the experimental results, **MAC\*-Cu-CzP** enantiomers exhibited higher $|g_{cal}|$ values (**Table 2**) than **MAC\*-Cu-CNCzP** enantiomers. This difference can be explained by the 1.3-fold higher $|m|$ value of $R_p$/$S_p$-**MAC\*-Cu-CzP** compared to $R_p$/$S_p$-**MAC\*-Cu-CNCzP**. To further clarify the crucial role of the chiral [2.2]paracyclophane moiety on the **$m$**, we decomposed the transition dipole moment vectors as atom contributions. As illustrated in **Figure 5E**, the **$m$** of $R_p$-**MAC\*-Cu-CzP** was mainly donated by the copper center, the N4 and C9 atoms of the MAC\* ligand, and the inner-ring carbon atoms (C89, C90, and C95) of the [2.2]paracyclophane moiety. As contrast, the contribution of the

benzene ring atoms (C79-C87-C85-C81) on the CzP ligand had opposite effect on $m$ and thus crippled the $|m|$ value of the complex. Differently, for $R_p$-MAC*-Cu-CNCzP (**Figure 5F**), the $m$ was mainly determined by the cyano-substituted benzene ring atoms (C79-C86-C84-C81) of the CNCzP ligand; whereas the inner-ring carbon atoms (C88, C89, and C94) on the [2.2]paracyclophane moiety had opposite effect to the $m$. In this context, the introduction of cyano group on the donor ligand could weaken chirality induced from the [2.2]paracyclophane moiety and reduce the $|m|$ value of $R_p$-MAC*-Cu-CNCzP, finally decreasing the $g$ value.
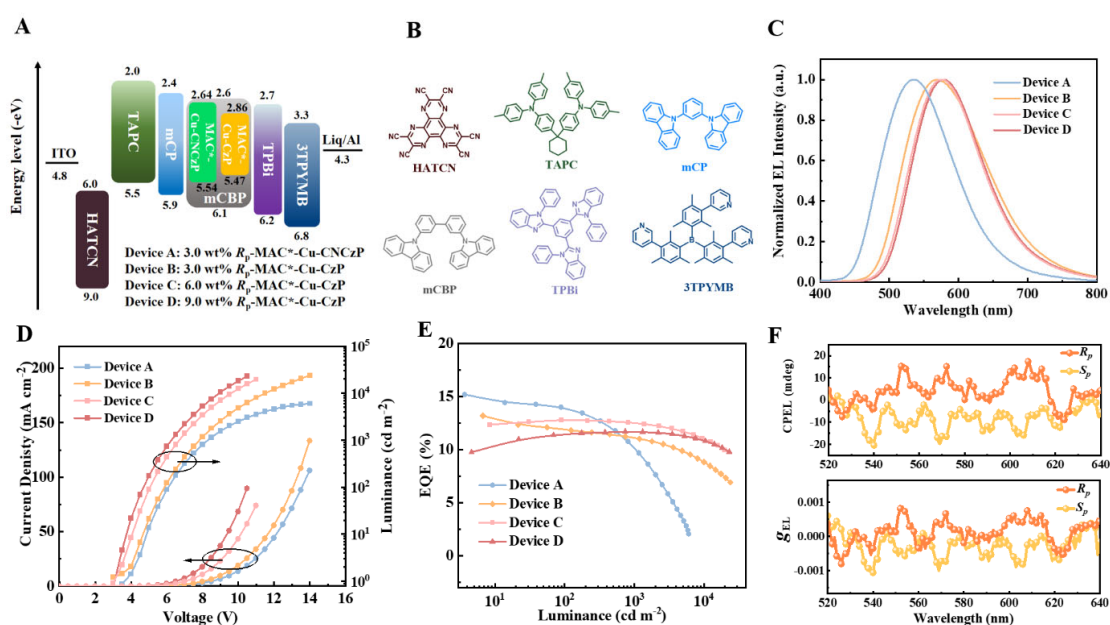


**Figure 6.** (A) Circular dichroism spectra of $R_p/S_p$-MAC*-Cu-CzP and $R_p/S_p$-MAC*-Cu-CNCzP in toluene ($10^{-3}$ M, 300 K). Circularly polarized luminescence spectra and photoluminescence dissymmetry factors of (B) $R_p/S_p$-MAC*-Cu-CzP and (C) $R_p/S_p$-MAC*-Cu-CNCzP in toluene ($10^{-4}$ M, 300 K). (D) Transition dipole moments and atom coordinates of $R_p$-MAC*-Cu-CzP and $R_p$-MAC*-Cu-CNCzP. Atomic contributions to the magnetic transition dipole moments of (E) $R_p$-MAC*-Cu-CzP and (F) $R_p$-MAC*-Cu-CNCzP.

**Table 3.** Summary of EL characteristics of the devices

| Device | $V_{on}$[a] [V] | $CE$[b] [cd A$^{-1}$] | $PE$[c] [lm W$^{-1}$] | $EQE$[d] [%] | Roll-off[e] [%] | $L_{max}$[f] [cd m$^{-2}$] | $EL_{peak}$ [nm] | CIE (x, y) |
|--------|------|------|------|------|------|------|------|------|
| A | 3.5 | 41.6, 38.1, 27.8 | 29.1, 19.8, 10.4 | 15.2, 13.7, 10.2 | 32.9, -- | 6017 | 510 | 0.34, 0.52 |
| B | 3.0 | 34.1, 31.1, 28.3 | 23.8, 16.3, 11.4 | 13.2, 12.0, 10.8 | 18.2, 34.8 | 23860 | 569 | 0.46, 0.51 |
| C | 3.0 | 34.2, 34.0, 33.2 | 25.9, 21.9, 16.0 | 12.8, 12.7, 12.5 | 2.3, 16.4 | 19720 | 579 | 0.47, 0.51 |
| D | 3.0 | 30.6, 30.5, 30.2 | 22.9, 20.6, 15.7 | 11.7, 11.6, 11.6 | 0.9, 7.7 | 23060 | 580 | 0.48, 0.50 |

[a] The turn-on voltage recorded at a luminance of 2 cd m$^{-2}$. Maximum values, values at 100 and 1000 cd m$^{-2}$ of [b] current efficiency, [c] power efficiency, and [d] external quantum efficiency. [e] External quantum efficiency roll-off at 1000 and 10000 cd m$^{-2}$. [f] Maximum luminance of the devices.

## CP-OLED Performance

To study the CPEL behavior and the EL performance of these complexes, typical multilayered OLEDs were fabricated. It consisted of indium tin oxide (ITO)/hexaazatriphenylene hexacarbonitrsile (HATCN) (5 nm)/1,1-bis[(di-4-tolylamino)phenyl]cyclohexane (TAPC) (60 nm)/*N,N*-dicarbazolyl-3,5-benzene (mCP) (10 nm)/emissive layer (25 nm)/2,2,2″-(l,3,5-benzenetriyl)-tris(*N*-phenyl-l-*H*-benzimidazole) TPBi (10 nm)/tris-[3-(3-pyridyl)mesityl]borane (3TPYMB) (50 nm)/Liq (1.5 nm)/Al (100 nm) (**Figure 6A** and **6B**). *R$_p$*-**MAC**$^*$-**Cu-CNCzP** (device A) and *R$_p$*-**MAC**$^*$-**Cu-CzP** (device B) were doped into the mCBP host with the optimal doping concentrations of 3.0 wt% to serve as the emissive layers. The devices based on the *S$_p$*-**MAC**$^*$-**Cu-CzP** (device E) and *S$_p$*-**MAC**$^*$-**Cu-CNCzP** (device F) were also fabricated for comparison (**Figure S15** and **Table S5**). Similar with the PL behaviors in the mCBP-doped films, the devices based on *R$_p$*-**MAC**$^*$-**Cu-CzP** and *R$_p$*-**MAC**$^*$-**Cu-CNCzP** exhibited yellow and green emissions peaking at 569 and 510 nm (**Figure 6C** and **Table 3**), respectively, together with favorable CIE1931 coordinates of (0.46, 0.51) and (0.34, 0.52). According to the current density-voltage-luminance curves (**Figure 6D**), the *R$_p$*-**MAC**$^*$-**Cu-CzP**-based device B had significantly lower turn-on voltage

(3.0 V) than that of the $R_p$-MAC$^*$-Cu-CNCzP-based device A (3.5 V), suggesting the more efficient charge carrier injection/transportation and better charge balance in the device B. Intriguingly, the optimal OLEDs based on $R_p$-MAC$^*$-Cu-CNCzP (device A) and $R_p$-MAC$^*$-Cu-CzP (device B) delivered outstanding device performance with the maximum EQEs of 15.2% and 13.2%, respectively (**Figure 6E** and **Table 3**). Similarly, $S_p$-MAC$^*$-Cu-CzP and $S_p$-MAC$^*$-Cu-CNCzP also supported their optimal devices E and F exhibiting maximum EQEs of 14.4% and 12.9%, respectively (**Figure S15** and **Table S5**). It is worth noting that with the increasing doping concentration from 3.0 to 9.0 wt%, the $R_p$-MAC$^*$-Cu-CzP-based devices B-D retained impressive EQEs of 11.7-13.2% along with slightly redshifted EL peaks from 569 to 580 nm. Thanks to the ultrafast RISC rate of $R_p$-MAC$^*$-Cu-CzP, the devices B-D manifested small efficiency roll-offs at high luminance. At a practical luminance of 1000 cd m$^{-2}$, the EQE of the device C only slightly dropped from 12.8% to 12.5% with a rather small EQE roll-off of 2.3%; even at an extremely high luminance of 10000 cd m$^{-2}$, the EQE remained as high as 11.2%. Furthermore, the device D (9.0 wt%) also exhibited ultraslow EQE roll-offs of 0.9% and 7.7% at the high luminance of 1000 and 10000 cd m$^{-2}$, respectively.

The CPEL characteristics were independently measured by the JASCO CPL-300 at the driving voltage of 5 V. As depicted in **Figure 6F**, the devices based on the $R_p/S_p$-MAC$^*$-Cu-CzP complexes exhibited distinct mirror-image CPEL signals with $g_{EL}$ values of +4.5 ×10$^{-4}$ and −5.9 ×10$^{-4}$ at 575 nm, respectively. These values are in the same order as the corresponding $g_{PL}$ values. In this context, the chirality can be transferred from the planar chiral donor ligand to these Cu(I)-CMA complexes both in

photoluminescence and electroluminescence processes. Combining with the maximum EQEs of nearly 13%, the $R_p/S_p$-**MAC***-**Cu-CzP**-based devices deliver one of the highest performances among all reported CP-OLEDs based on earth-abundant metal complexes. To the best of our knowledge, this work also demonstrates the first example of CP-OLEDs based on chiral CMA complexes.

**Conclusion**

In summary, we have developed two pairs of Cu(I)-based thermally activated delayed fluorescence (TADF) enantiomers of $R_p/S_p$-**MAC***-**Cu-CzP** and $R_p/S_p$-**MAC***-**Cu-CNCzP** bearing the [2.2]paracyclophane-based carbazole ligands. The presence of the [2.2]paracyclophane moiety not only brought the chirality source, but also lead to a twisted conformation between the carbene and amide ligands. Consequently, these complexes exhibited ultrafast reverse intersystem crossing rates of up to $10^8$ s$^{-1}$ in solution. Impressively, **MAC***-**Cu-CzP** exhibited distinct TADF emission with short lifetime and large radiative rate constant; whereas **MAC***-**Cu-CNCzP** displayed dual emission channels with large TADF character and partial phosphorescence feature. Notably, $R_p/S_p$-**MAC***-**Cu-CzP** exhibited distinct circularly polarized luminescence (CPL) signal with photoluminescence dissymmetry factors in the $10^{-4}$ order. Comparatively, **MAC***-**Cu-CNCzP** enantiomers displayed significantly poor CPL properties, which could originate from the smaller values of magnetic transition dipole moments. Accordingly, the CP-OLEDs based on $R_p/S_p$-**MAC***-**Cu-CzP** exhibited obvious circularly polarized electroluminescence signals with electroluminescence

dissymmetry factors of $+4.5\times10^{-4}$ and $-5.9\times10^{-4}$, respectively. More importantly, the optimal CP-OLEDs based on **MAC*-Cu-CzP** enantiomers exhibited the maximum EQE of 13.2% and delivered the extremely small efficiency roll-off of 7.7% at high luminance of 10000 cd m$^{-2}$, representing one of the highest efficiencies for CP-OLEDs based on earth-abundant organometallic complexes. This work not only demonstrates the first example of efficient CP-OLEDs from CMA complexes, but also unlocks the large potential of luminescent Cu(I) complexes for high-performance and low-cost CP-OLEDs.

## References
[1] J. Han, S. Guo, H. Lu, S. Liu, Q. Zhao, W. Huang, *Adv. Opt. Mater.* **2018**, *6*, 1800538.
[2] J. R. Brandt, F. Salerno, M. J. Fuchter, *Nat. Rev. Chem.* **2017**, *1*, 0045.
[3] D.-W. Zhang, M. Li, C.-F. Chen, *Chem. Soc. Rev.* **2020**, *49*, 1331-1343.
[4] D. Parker, J. D. Fradgley, K.-L. Wong, *Chem. Soc. Rev.* **2021**, *50*, 8193-8213.
[5] F. Zinna, L. D. Bari, *Chirality* **2015**, *27*, 1-13.
[6] J. Crassous, *Chem. Soc. Rev.* **2009**, *38*, 830-845.
[7] C. Bizzarri, E. Spuling, D. M. Knoll, D. Volz, S. Brase, *Coord. Chem. Rev.* **2018**, *373*, 49-82.
[8] J. OuYang, J. Crassous, *Coord. Chem. Rev.* **2018**, *376*, 533-547.
[9] G. Lu, Z.-G. Wu, R. Wu, X. Cao, L. Zhou, Y.-X. Zheng, C. Yang, *Adv. Funct. Mater.* **2021**, *31*, 2102898.

[10] Z.-P. Yan, X.-F. Luo, W.-Q. Liu, Z.-G. Wu, X. Liang, K. Liao, Y. Wang, Y.-X. Zheng, L. Zhou, J.-L. Zuo, Y. Pan, H. Zhang, *Chem. Eur. J.* **2019**, *25*, 5672-5676.

[11] F. Zinna, U. Giovanella, L. D. Bari, *Adv. Mater.* **2015**, *27*, 1791-1795.

[12] C. B. Larsen, O. S. Wenger, *Chem. Eur. J.* **2018**, *24*, 2039-2058.

[13] A. Hossain, A. Bhattacharyya, O. Reiser, *Science* **2019**, *364,* eeav9713.

[14] S. S. Xue, Y. Pan, W. Pan, S. Liu, N. Li, B. Tang, *Chem. Sci.* **2022**, *13*, 9468-9484.

[15] J. Troyano, F. Zamora, S. Delgado, *Chem. Soc. Rev.* **2021**, *50*, 4606-4628.

[16] C. Sun, B. K. Teo, C. Deng, J. Lin, G.-G. Luo, C.-H. Tung, D. Sun, *Coord. Chem. Rev.* **2021**, *427*, 213576.

[17] Y. Chen, X. Li, N. Li, Y. Quan, Y. Cheng, Y. Tang, *Mater. Chem. Front.* **2019**, *3*, 867-873.

[18] M. Deng, N. F. M. Mukthar, N. D. Schley, G. Ung, *Angew. Chem. Int. Ed.* **2020**, *59*, 1228-1231.

[19] A. M. T. Muthig, O. Mrózek, T. Ferschke, M. Rödel, B. Ewald, J. Kuhnt, C. Lenczyk, J. Pflaum, A. Steffen, *J. Am. Chem. Soc.* **2023**, DOI: 10.1021/jacs.2c09458.

[20] D. Di, A. S. Romanov, L. Yang, J. M. Richter, J. P. Rivett, S. Jones, T. H. Thomas, M. A. Jalebi, R. H. Friend, M. Linnolahti, *Science* **2017**, *356*, 159-163.

[21] R. Hamze, J. L. Peltier, D. Sylvinson, M. Jung, J. Cardenas, R. Haiges, M. Soleilhavoup, R. Jazzar, P. I. Djurovich, G. Bertrand, M. E. Thompson, *Science* **2019**, *363*, 601-606.

[22] A. S. Romanov, S. T. E. Jones, Q. Gu, P. J. Conaghan, B. H. Drummond, J. Feng, F. Chotard, L. Buizza, M. Foley, M. Linnolahti, D. Credgington, M. Bochmann, *Chem. Sci.* **2020**, *11*, 435-446.

[23] S. Shi, M. C. Jung, C. Coburn, A. Tadle, M. R. D. Sylvinson, P. I. Djurovich, S. R. Forrest, M. E. Thompson, *J. Am. Chem. Soc.* **2019**, *141*, 3576-3588.

[24] M. Gernert, L. Balles-Wolf, F. Kerner, U. Muller, A. Schmiedel, M. Holzapfel, C. M. Marian, J. Pflaum, C. Lambert, A. Steffen, *J. Am. Chem. Soc.* **2020**, *142*, 8897-8909.

[25] C. N. Muniz, J. Schaab, A. Razgoniaev, P. I. Djurovich, M. E. Thompson, *J. Am. Chem. Soc.* **2022**, *144*, 17916-17928.

[26] A. Ying, Y.-H. Huang, C.-H. Lu, Z. Chen, W.-K. Lee, X. Zeng, T. Chen, X. Cao, C.-C. Wu, S. Gong, C. Yang, *ACS Appl. Mater. Interfaces* **2021**, *13*, 13478-13486.

[27] P. J. Conaghan, C. S. B. Matthews, F. Chortard, S. T. E. Jones, N. C. Greenham, M. Bochmann, D. Credgington, A. S. Romanov, *Nat. Commun.* **2020**, *11*, 1758-1765.

[28] A. Ruduss, B. Turovska, S. Belyakov, K. A. Stucere, A. Vembris, G. Baryshnikov, H. Agren, J.-C. Lu, W.-H. Lin, C.-H. Chang, K. Traskovskis, *ACS Appl. Mater. Interfaces* **2022**, *14*, 15478-15493.

[29] R. Tang, S. Xu, T.-L. Lam, G. Cheng, L. Du, Q. Wan, J. Yang, F.-F. Hung, K. H. Low, D. L. Phillips, C.-M. Che, *Angew. Chem. Int. Ed.* **2022**, *61*, e202203982.

[30] H.-J. Wang, Y. Liu, B. Yu, S.-Q. Song, Y.-X. Zheng, K. Liu, P. Chen, H. Wang, J. Jiang, T.-Y. Li, *Angew. Chem. Int. Ed.* **2022**, *62*, e202217195; *Angew. Chem.* **2022**, *135*, e202217195.

[31] J. P. Zobel, A. Wernbacher, L. Gonzalez, *Angew. Chem. Int. Ed.* **2023**, e202217620.

[32] A. Ying, Y. Ai, C. Yang, S. Gong, *Angew. Chem. Int. Ed.* **2022**, *61*, e202210490.

[33] R. Lopez, C. Palomo, *Angew. Chem. Int. Ed.* **2022**, *61*, e202113504.

[34] N. Sharma, E. Spuling, C. M. Mattern, W. Li, O. Fuhr, Y. Tsuchiya, C. Adachi, S. Brase, I. D. W. Samuel, E. Zysman-Colman, *Chem. Sci.* **2019**, *10*, 6689-6696.

[35] C. Liao, Y. Zhang, S.-H. Ye, W.-H. Zheng, *ACS Appl. Mater. Interfaces* **2021**, *13*, 25186-25192.

[36] X.-J. Liao, D. Pu, L. Yuan, J. Tong, S. Xing, Z.-L.Tu, J.-L. Zuo, W.-H. Zheng, Y.-X. Zheng, *Angew. Chem. Int. Ed.* **2023**, *62*, e202217045.

[37] Deposition numbers 2077848 (for $R_P$-MAC*-Cu-CzP) and 2077850 (for $R_P$-MAC*-Cu-CNCzP) contain the supplementary crystallographic data for this paper. These data are provided free of charge by the joint Cambridge Crystallographic Data Centre Access Structures.

[38] J. Li, L. Wang, Z. Zhao, X. Li, X. Yu, P. Huo, Q. Jin, Z. Liu, Z. Bian, C. Huang, *Angew. Chem. Int. Ed.* **2020**, *59*, 8210-8217.

[39] J. Feng, A. P. M. Reponen, A. S. Romanov, M. Linnolahti, M. Bochmann, N. C. Greenham, T. Penfold, D. Credgington, *Adv. Funct. Mater.* **2020**, *31*, 2005438.

[40] J. Feng, E. J. Taffet, A.-P. M. Reponen, A. S. Romanov, Y. Olivier, V. Lemaur, L. Yang, M. Linnolahti, M. Bochmann, D. Beljonne, D. Credgington, *Chem. Mater.* **2020**, *32*, 4743-4753.

[41] F. Ni, C.-W. Huang, Y. Tang, Z. Chen, Y. Wu, S. Xia, X. Cao, J.-H. Hsu, W.-K. Lee, K. Zheng, Z. Huang, C.-C. Wu, C. Yang, *Mater. Horiz.* **2021**, *8*, 547.